

Radio frequency sheaths in an oblique magnetic field

J. R. Myra and D. A. D'Ippolito

Lodestar Research Corporation, Boulder, CO, USA

April 2015

submitted to *Physics of Plasmas*

DOE-ER/54392-77

LRC-15-161

LODESTAR RESEARCH CORPORATION

2400 Central Avenue
Boulder, Colorado 80301

Radio frequency sheaths in an oblique magnetic field

J. R. Myra and D. A. D'Ippolito

Lodestar Research Corporation, 2400 Central Avenue, Boulder, Colorado 80301

Abstract

The physics of radio-frequency (rf) sheaths near a conducting surface is studied for plasmas immersed in a magnetic field that makes an oblique angle θ with the surface. A set of one-dimensional equations is developed that describe the dynamics of the time-dependent magnetic presheath and non-neutral Debye sheath. The model employs Maxwell-Boltzmann electrons, and the magnetization and mobility of the ions is determined by the magnetic field strength, and wave frequency, respectively. The angle θ , assumed to be large enough to insure an electron-poor sheath, is otherwise arbitrary. Concentrating on the ion-cyclotron range of frequencies, the equations are solved numerically to obtain the rectified (dc) voltage, the rf voltage across the sheath and the rf current flowing through the sheath. As an application of this model, the sheath voltage-current relation is used to obtain the rf sheath impedance, which in turn gives an rf sheath boundary condition for the electric field at the sheath-plasma interface that can be used in rf wave codes. In general the impedance has both resistive and capacitive contributions, and generalizes previous sheath boundary condition models. The resistive part contributes to parasitic power dissipation at the wall.

PACS numbers: 52.40.Kh, 52.35.Mw, 52.50.Qt, 52.55.Fa

I. Introduction

The subject of radio-frequency (rf) sheaths is important for ion cyclotron range of frequency (ICRF) heating and current drive in fusion experiments. It should be emphasized that ICRF wave coupling to the core plasma has been successful in many experiments and is expected to play an important role in ITER. However, ICRF waves can drive rf sheaths on the antenna and other boundary surfaces, and these sheaths can sometimes produce a number of unwanted interactions such as rf-enhanced impurity sputtering and self-sputtering, parasitic power dissipation, hot spots, and reduced heating efficiency of the core plasma. Minimizing these interactions is important to the success of rf heating, especially in future experiments with long-pulse or steady-state operation, higher power density, and high-Z divertor and walls. Reviews of experimental and theoretical work on ICRF edge and wall interactions are given in Refs. 1-2 and a short overview of the physics can be found in Ref. 3. More recently, these issues have been the subject of experimental investigations on many tokamaks,⁴⁻¹² and have given rise to a number of dedicated modeling efforts.¹³⁻²⁰

The origin of rf sheaths in fusion experiments is well known.^{1,21-23} Most ICRF antennas used in present experiments are designed to launch the fast wave (FW), which has the polarization $E_{\parallel} \approx 0$. (Here, E_{\parallel} is the component of the rf electric field that is parallel to the equilibrium magnetic field.) When the current straps of the antenna are not perfectly aligned perpendicular to the magnetic field, it can also couple to the slow wave (SW) which has $E_{\parallel} \neq 0$,²⁴ a fact that is well recognized in modern antenna designs.^{4,5} On field lines that intersect the antenna or other material boundaries, the SW accelerates electrons out of the plasma producing a large rectified (dc) sheath potential to maintain ambipolarity. This potential confines electrons and accelerates ions out of the plasma into the boundary, leading to the unwanted interactions listed above. For high-power ICRF heating experiments, the rf sheath potential near the antenna is typically much larger than the Bohm (thermal) sheath potential, i.e. $eV_{\text{rf}} \gg 3T_e$. (Here and in the following dimensional temperatures are expressed in units of electron volts.)

Another situation in which large rf potentials can develop is FW heating with low single pass absorption.^{25,26} In this case, the FW can propagate into distant walls and limiters, and must couple to the SW in order to satisfy the metal wall BC derived from Maxwell equations, viz. $E_t = 0$, where t denotes the component “tangential” to the wall. In both the antenna sheath and far-field sheath cases, the strength of the rf sheath potential depends on the rf wave polarization and on the degree of misalignment between the background magnetic field and the antenna or other conducting boundary. Thus, the rf sheath potential varies from field line to field line and is

sensitive to the B field and wall geometry. Because of this sensitivity, it is hard to do simple estimates of the sheath potential; quantitative modeling is needed.

One approach to calculating the self-consistent rf sheath potential from an rf wave code is the use of an rf sheath boundary condition (BC)^{25,27} at the sheath-plasma interface. In this work, the sheath BC was an extension of the metal wall BC to include the effect of sheath capacitance. (A similar BC was developed for simulations of plasma processing in Ref. 28.) The sheath is treated as a thin vacuum layer separating the metal boundary and the plasma. The rf sheath BC is derived from the continuity of the normal component of $\mathbf{D} = \boldsymbol{\epsilon} \cdot \mathbf{E}$ (where $\boldsymbol{\epsilon}$ is the rf dielectric tensor) and of the tangential components of the electric field \mathbf{E} across the plasma-sheath interface. When combined with the Child-Langmuir scaling of the sheath width, the sheath BC becomes nonlinear and can produce multiple roots for the sheath potential in a variety of problems (e.g. see examples in Refs. 17-19 and 26). The additional roots result from the effect of the sheath capacitance and have much larger sheath potentials than expected from simple estimates. One of the goals of the present paper is to generalize the rf sheath BC to include the total (i.e. resistive plus capacitive) impedance in order to also calculate the sheath power dissipation self-consistently. It is expected that this generalization may be of interest in ongoing modeling efforts that employ an rf sheath boundary condition formulation.^{13,14,19,20}

A detailed discussion of rf sheath regimes was given in an earlier paper²² and a study of sheath rectification was carried out. The sheath equations for the general case were written down and the structure of the sheath and magnetic presheath regions in different limits was discussed. The simplest case is that of strongly magnetized ions in the sheath, Maxwell-Boltzmann electrons in the sheath and presheath, and B fields normal to the sheath. In this limit, the sheath impedance is capacitive and the dominant current across the sheath is the displacement current. There is no magnetic presheath when the ions are strongly magnetized, i.e. in the limit $\rho_i \ll \lambda_d$ where ρ_i is the ion gyro-radius and λ_d is the Debye length. Most of the sheath modeling for ICRF antennas has used this model. In the ICRF regime, where $\omega \sim \Omega_i$ the strongly magnetized ion limit corresponds to $\omega \gg \omega_{pi}$ where ω is the wave frequency and ω_{pi} is the ion plasma frequency. This limit also corresponds to the “immobile” ion limit for which ion inertia prevents large jitter excursions. In the present work, we solve other limits of the general case (varying the B field angle, ion magnetization, mobility, etc.) to get a broader picture, similar to the goals of Ref. 16. However, the main achievement of the present work is that in each case, the rf sheath impedance is extracted from the numerical sheath solution and used to evaluate the rf sheath BC.

The generality of the present setting allows a greatly improved treatment of rf-sheath interactions in the tokamak scrape-off layer (SOL) while still maintaining the advantages, in a global wave code, of employing a boundary condition approach. For example, in the SOL the magnetic field angle varies from perpendicular to nearly parallel around a limiter.¹⁹ The density

(and hence the ion mobility) also shows strong radial variation across the SOL. Thus, the usual sheath model needs to be extended, as described in this paper, to give a more accurate description of rf sheaths in tokamak plasmas.

In summary, the main goal of this paper is to use a numerical approach to study the general rf sheath solution. The new results are the following:

- a set of model equations, and corresponding numerical solutions, describing the dynamics of rf sheaths in an oblique magnetic field for a wide range of parameters;
- an expression for, and numerical characterization of, the complex sheath impedance (resistive and capacitive parts) and rectified sheath voltage evaluated from the sheath solution;
- an expression for the generalized rf sheath boundary condition in terms of the sheath impedance.

The plan of this paper is as follows. In Sec. II we describe the equations that determine the structure of the plasma in the vicinity of the sheath surface. The numerical solution of these equations over a wide range of parameters (rf driving voltage, magnetic field angle, ion magnetization and ion mobility) is discussed in Sec. III. The role of the magnetic presheath for oblique angle rf sheaths is illustrated, and it is shown that for $\omega \sim \omega_{pi}$ the non-neutral rf sheath can generate Debye scale oscillations distinct from, but reminiscent of the sheath plasma wave (SPW).^{20,29-31} In Sec. IV we show how the sheath model can be used to calculate the sheath impedance and a generalized form of the rf sheath BC used in rf wave propagation codes. The new approach expresses the BC at the sheath-plasma interface (i.e. where the main plasma meets the magnetic presheath) in terms of the complex sheath impedance, including both resistive and capacitive effects. In Sec. V the dependence of the rf sheath impedance on parameters is shown, and a summary of the main results of this paper and our conclusions are discussed in Sec. VI. The dimensionless equations used in the numerical work are listed in Appendix A, and a model for sheath-driven waves is briefly discussed in Appendix B. Finally, in Appendix C sheath energy conservation is discussed. It is shown that the Poynting flux of the wave propagating into the sheath equals the sheath power loss when the proper sheath BC is used.

II. Sheath model equations

In this section we describe a numerical model of the 1D electrostatic rf sheath in a plasma-filled parallel-plate model, which generalizes our previous model²² to include the effects of arbitrary ion magnetization, ion mobility and arbitrary magnetic field angle with respect to the

sheath. Viewed another way, this work generalizes work on steady state (dc) oblique angle sheaths and the magnetic presheath³²⁻³⁹ to include rf sheath effects.

We consider the following model problem. Let x be the coordinate normal to the sheaths on two parallel plates in the y - z plane located at $x = x_1$ and x_2 . Thus the plasma domain is $x_1 < x < x_2$. Assume that straight field lines connect the two plates, and define the angle θ between the magnetic field line and the plate such that $\theta = 0$ ($\theta = \pi/2$) corresponds to a field line parallel (perpendicular) to the surface of the plate. For brevity, we will refer to this as “the magnetic field angle” in this paper. This B-field angle is assumed to be large enough to yield an electron-poor sheath. [This condition is $(m_e/m_i)^{1/2} < \sin \theta$ for $eV_{rf} \leq 3T_e$ but is more relaxed in strongly rf driven cases.] Finally, we define a non-orthogonal coordinate system with unit vectors (\mathbf{s}, \mathbf{b}) , where $\mathbf{s} = \hat{\mathbf{e}}_x$ is the unit vector normal to the sheath surface, $\mathbf{b} = \mathbf{B}/B$ is the unit vector parallel to the B field, and we let $\mathbf{p} = \mathbf{b} \times \mathbf{s}$. Note that \mathbf{p} is not a unit vector.

The complete description (allowing treatment of both the magnetized and unmagnetized ion limits) requires Poisson’s equation, the ion continuity equation and momentum equations for the three components of the ion velocity. The Maxwell-Boltzmann approximation is made for the electrons and is expected to be valid when $\omega L_x < v_{te} b_x$ where L_x is a characteristic scale length normal to the sheath surface, and v_{te} is the electron thermal velocity. The resulting set of dimensional equations is

$$\frac{\partial^2 \Phi}{\partial x^2} = -4\pi e(n_i - n_e), \quad (1)$$

$$n_e = n_0 \exp[e(\Phi - \Phi_0)/T], \quad (2)$$

$$\frac{\partial n_i}{\partial t} + \frac{\partial}{\partial x}(n_i u_x) = 0, \quad (3)$$

$$\frac{1}{\Omega} \left(\frac{\partial}{\partial t} + u_x \frac{\partial}{\partial x} \right) u_x = v_E + u_p, \quad (4)$$

$$\frac{1}{\Omega} \left(\frac{\partial}{\partial t} + u_x \frac{\partial}{\partial x} \right) u_p = u_{\parallel} b_x - u_x, \quad (5)$$

$$\frac{1}{\Omega} \left(\frac{\partial}{\partial t} + u_x \frac{\partial}{\partial x} \right) u_{\parallel} = v_E b_x, \quad (6)$$

where $u_{\parallel} = \mathbf{u} \cdot \mathbf{b}$, $u_p = \mathbf{u} \cdot \mathbf{p} = \mathbf{u} \cdot \mathbf{b} \times \mathbf{s}$, $b_x = \mathbf{b} \cdot \mathbf{e}_x = \mathbf{b} \cdot \mathbf{s}$ and

$$v_E = -\frac{Ze}{m\Omega} \frac{\partial \Phi}{\partial x} \quad (7)$$

is the local rf jitter velocity. Here, m is the ion mass, Z is the charge state, Ω is the ion cyclotron frequency, $\Phi(x,t)$ is the electrostatic potential, $\mathbf{u}(x,t)$ is the ion velocity, and a subscript 0 indicates upstream values far from the sheath, in practice evaluated at the midpoint of the domain. The ion and electron plasma densities are $n_i(x,t)$ and $n_e(x,t)$ respectively, and $T = T_e$ is the (constant) electron temperature.

The boundary conditions and constraints are

$$\Phi(x_1) = V_1 = \frac{V_{pp}}{2} \cos \omega t \quad (8)$$

$$\Phi(x_2) = V_2 = -\frac{V_{pp}}{2} \cos \omega t \quad (9)$$

$$J_{x1} - J_{x2} = 0 \quad (10)$$

$$J_{x1} = Zen_{i1}u_1 - \frac{\sigma_1 e v_e}{(2\pi)^{1/2}} b_x n_0 \exp[e(V_1 - \Phi_0)/T] - \frac{1}{4\pi} \frac{\partial^2 \Phi_1}{\partial t \partial x} \quad (11)$$

Here, V_{pp} is the peak-to-peak amplitude of the applied oscillating voltage, and V_1 and V_2 are the instantaneous voltages on the two plates. J_{x1} is the current at $x = x_1$, defined to be positive when the current is in the positive x direction, i.e. when current (+charge) is leaving the x_1 surface and flowing into the plasma and v_e is the electron thermal velocity. Thus, $\sigma_1 = -1$ and we anticipate $u_1 < 0$. J_{x2} appearing in Eq. (10) is obtained from the symmetry relations discussed next.

For numerical work it is useful to carry out the solution on the half domain $(0, L)$ defined by $x_1 = 0$ and $L = (x_1 + x_2)/2$ using the following symmetries:

$$V_{x2}(\omega t) = V_{x1}(\omega t + \pi), \quad (12)$$

$$n_{x2}(\omega t) = n_{x1}(\omega t + \pi), \quad (13)$$

$$u_{x2}(\omega t) = -u_{x1}(\omega t + \pi), \quad (14)$$

$$J_{x2}(\omega t) = -J_{x1}(\omega t + \pi), \quad (15)$$

$$\Phi_{x2}(\omega t) = \Phi_{x1}(\omega t + \pi), \quad (16)$$

$$\partial_x \Phi_{x2}(\omega t) = -\partial_x \Phi_{x1}(\omega t + \pi), \quad (17)$$

$$\sigma_2 = -\sigma_1. \quad (18)$$

Thus, the current constraint can be written as

$$J_{x1} + J_{x1}(\omega t + \pi) = 0. \quad (19)$$

As a consequence of Eq. (10) which requires that the instantaneous current collected from one plate be delivered to the other plate by a closed circuit, there is also an ambipolarity condition: there can be no buildup of net charge. Thus, the time-average of Eq. (11), the net current leaving the system, must vanish

$$Ze \langle n_{i1} u_{x1} \rangle - \frac{\sigma_1 e v_e}{(2\pi)^{1/2}} b_x n_0 \langle \exp[e(V_1 - \Phi_0)/T] \rangle = 0, \quad (20)$$

where $\langle Q \rangle$ denotes the time-average of Q . Note that $\langle n_{i1} u_{x1} \rangle = n_0 u_{x0}$ from the time-averaged continuity equation.

The sheath equations can be cast in *dimensionless* form by normalizing time to ω_{pi0}^{-1} and distance to the Debye length, $\lambda_{d0} = (T_e/4\pi n_0 e^2)^{1/2}$, which is the natural scale length of the non-neutral sheath. The complete set of dimensionless variables is

$$\begin{aligned} \hat{L} &= L/\lambda_{d0}, \quad \hat{t} = \omega_{pi0} t, \quad \hat{u} = u/c_s, \quad \hat{n} = n/n_0, \quad \hat{J} = J/(n_0 e c_s), \\ \hat{V} &= eV/T_e, \quad \hat{\Phi} = e\Phi/T_e, \quad \hat{z} = z\omega_{pi0}/(4\pi\lambda_{d0}). \end{aligned} \quad (21)$$

Here n_0 is the density upstream of the sheath (at the symmetry plane), T_e is the (constant) electron temperature, $c_s = (T_e/m_i)^{1/2}$ and z is a sheath impedance parameter that will be introduced in latter sections. The corresponding dimensionless equations are given in Appendix A, and their solutions are discussed in Sec. III.

Finally, note that the dimensionless ion cyclotron frequency

$$\hat{\Omega} = \frac{\Omega}{\omega_{pi0}} = \frac{\lambda_{d0}}{\rho_s} \quad (22)$$

is the ion *magnetization parameter*. In the limit $\hat{\Omega} \ll 1$ the ions are not strongly magnetized and a magnetic presheath of scale length $\rho_s \gg \lambda_{d0}$ is formed, whereas for $\hat{\Omega} \gg 1$ the ions are strongly magnetized and there is no magnetic presheath. The *ion mobility parameter* is $\hat{\omega} = \omega/\omega_{pi0}$. The ions are immobile for large $\hat{\omega}$ (i.e. their inertia prevents much response to the driving wave, in particular the ions cannot transit the sheath in a wave period) and mobile for small $\hat{\omega}$. For ICRF heating, $\omega \sim \Omega$ so that $\hat{\omega} \sim \hat{\Omega}$. Thus, for ICRF, strongly magnetized ions

tend to be immobile and weakly magnetized ions are mobile. Previous characterizations of the sheath response, valid in the capacitive limit, correspond to $\hat{\Omega} \gg 1$ and $\hat{\omega} \gg 1$. The present model allows the entire range of $\hat{\Omega}$ and $\hat{\omega}$ to be explored.

III. Numerical solutions

The dimensionless versions of Eqs. (1) – (6), together with the constraints (8) – (11), (20) and associated definitions have been implemented in a MathematicaTM code on the spatial domain (0, L). These equations are differential in space and integro-differential in time. [Eq. (20) involves a time integral; it is redundant, being derivable from Eqs. (10) and (11), but nonetheless useful in the numerical implementation. In the high frequency limit the largest term in Eq. (11) $\sim \partial_t \partial_x \Phi_1$ is annihilated by the time average; consequently use of Eq. (20) insures numerical accuracy of the time-averaged ambipolarity condition.] The equations were discretized in both x and t variables using second-order accurate finite difference operators in the volume region with N spatial points and M time points. In the numerical implementation, Eq. (10) was applied at M–1 time points supplemented by the time-average given in Eq. (20), performed as an unweighted mean. This discretization procedure resulted in a non-linear root-finding problem in an abstract space of dimension N×M. The nonlinear root-finding was then accomplished by standard techniques, which are variants of the secant method. If a good guess was provided, root-finding convergence to machine precision was routinely obtained. An alternative numerical method would be to time advance the equations, probably with some dissipation, until the system relaxes into a periodic state. This method, not explored here, would likely require integration over a very large number of rf cycles in some regimes.

Several strategies for initial root-finding guesses, used in combination, were found to be successful. The basic idea is to start with a trivial case for which the solution is known or easily obtained, and then use it to track, step by step, to a solution for the desired parameters. A useful starting point is the dc sheath ($\hat{\omega} = 0$ or $\hat{V}_{pp} = 0$) for which one can take M = 2. (M = 1 is not possible for the particular discretization scheme employed.) A second strategy is to start with a low resolution grid to obtain a rough solution, and then use it (interpolated onto a higher resolution grid) as a guess. Convergence of results to a relative accuracy of 0.01 or better as N and M are increased typically requires N = 50 and M = 80 and requires on the order of a few hours on a single processor to track from $\hat{V}_{pp} = 0$ to $\hat{V}_{pp} = 20$. Cases as large as N = 200 and M = 160 (not simultaneously) have been run to check numerical accuracy.

For the remainder of this section, results will be presented in dimensionless variables, and carets denoting dimensionless quantities will be dropped where there can be no confusion.

Figure 1 shows a typical result for the space-time variation of the fields for a case that is marginally mobile and not strongly magnetized. This case is not in the purely capacitive limit, as we shall see, but rather illustrates a more general case where the physics of the magnetic presheath is evident. Dimensionless parameters are $\Omega=0.1$, $b_x=0.2$, $\omega=0.3$, $V_{pp}=20$ together with the boundary conditions $n_0 = 1$, $u_{\parallel 0} = -1.1$, $u_{x0} = b_x u_{\parallel 0}$, $u_{p0} = 0$ and $[m_i/(2\pi m_e)]^{1/2} = 23.9$. The preceding set of boundary conditions is used for all of the results presented in this paper.

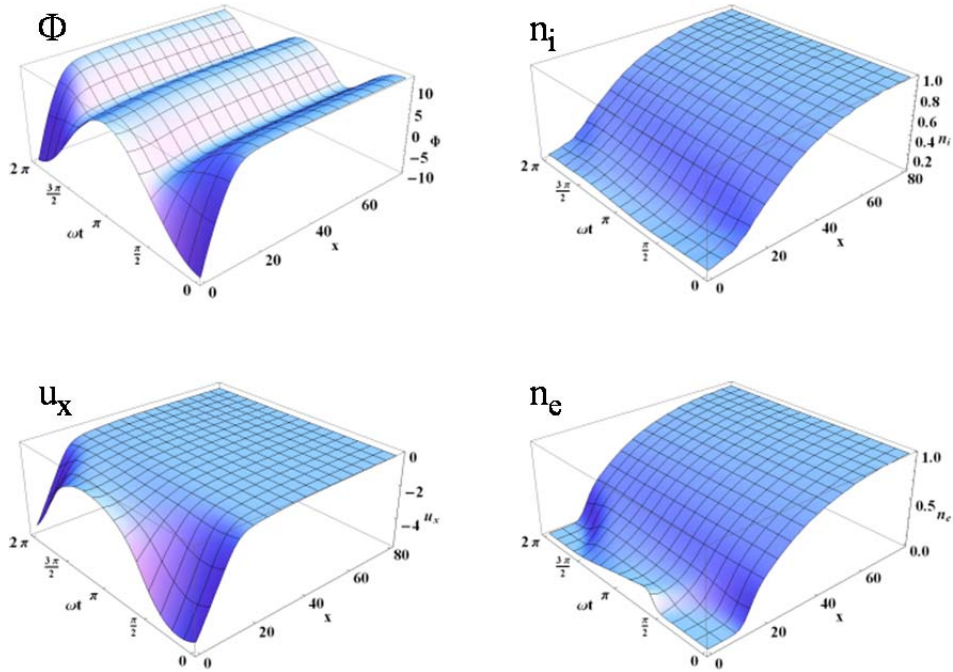


Fig. 1. Space-time plots of dimensionless rf-sheath quantities for case (a) of Table I: $\Omega=0.1$, $b_x=0.2$, $\omega=0.3$, $V_{pp}=20$ which is a marginally mobile, weakly magnetized glancing angle sheath. Shown clock-wise from upper left are the electrostatic potential, ion density, electron density and velocity normal to the wall. The wall, $x = 0$, is at the left and time (i.e. wave phase ωt) advances in the direction receding to the left into the page.

Rectification in Fig. 1 is evident by comparing the time-average potential at the wall $x = 0$, viz. $\langle \Phi \rangle_t = 0$ with the upstream average potential $\langle \Phi \rangle_t \sim 10$. During the high voltage part of the cycle, near the wall the scale length of the potential is a few λ_d . In contrast, the ion density decreases towards the wall on a much longer scale of order several ρ_s where $\rho_s = 10$ (in units of λ_{d0} since $\hat{\Omega} = 0.1$). The electron density provides quasi-neutrality in the magnetic presheath, but drops quickly to zero in the non-neutral sheath during the high voltage part of the cycle. (See also Fig. 2) The plasma flow, u_x , shows strong acceleration towards the wall ($u_x < 0$), especially during the high voltage part of the cycle.

A more detailed examination of the results for the same case is shown in the left panels of Fig. 2. These spatial profiles are taken at the time of maximum applied voltage, $V_{pp} = 20$. From the top panel, we see that the short scale Debye (non-neutral) sheath has an extent of about $20 \lambda_{d0}$. This is on the order of the Child-Langmuir (CL) sheath width given by $\Delta = \lambda_d (eV/T)^{3/4} \sim 9.5 \lambda_{d0}$ but note that the actual density at the location of the Debye sheath increases the local λ_d by a factor of order $n_i^{-1/2} \sim 0.2^{-1/2} = 2.2$ (see lower panel) so that the local CL law gives $\Delta \sim 21 \lambda_d$ as observed.

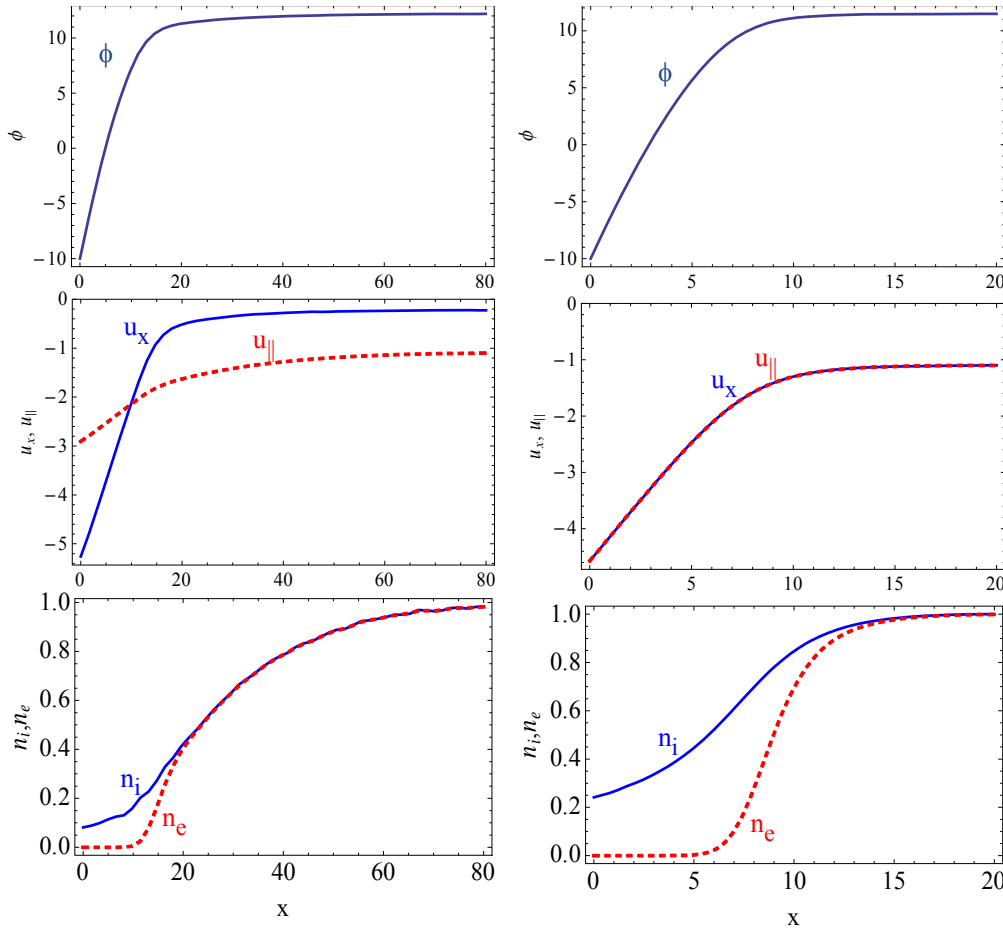


Fig. 2. Spatial profiles at the time of maximum applied rf voltage ($t = 0$, $V_{pp} = 20$) for two cases: left panel is case (a), of Table 1, i.e. the case Fig. 1, right panel is case (e) for which $b_x=1$, $\omega=9$. The latter case is a perpendicular sheath (Ω is irrelevant) which is in the immobile regime. Note the difference in the scale of x . The panels, top to bottom are: electrostatic potential, velocity components normal to the wall (blue) and parallel to B (red-dashed), and ion (blue) and electron (red-dashed) density. All quantities are dimensionless.

Upstream (in the left panels of Fig. 2) where the ions are locally magnetized because the scale lengths greatly exceed ρ_s , the flow starts out mostly parallel but at $x \sim 15 \lambda_{d0}$, near the boundary between the magnetic presheath and the non-neutral sheath, u_x overtakes u_{\parallel} as the ions become demagnetized and flow directly into the wall. Quasi-neutrality holds in the magnetic presheath ($x > 20 \lambda_{d0}$) but not in the Debye sheath. All of these features are well known for static sheaths in a magnetic field making an oblique angle with a wall.³²⁻³⁴ The present results serve to show that they also hold qualitatively for rf sheaths here. This is to be expected by comparing the time and convective derivative on the left-hand-side of Eqs. (4)–(6): $\partial_t \sim \omega$ while in the magnetic presheath $u_x \partial_x \sim c_s \rho_s = \Omega$; consequently, for $\hat{\omega} < 1$ time derivatives do not dominate the convective derivatives. In the opposite, immobile limit $\hat{\omega} > 1$, the ions basically respond on the dc time-scale only.

The right panels of Fig. 2 show a contrasting case (e) from Table 1, viz. a perpendicular sheath which is in the immobile ($\hat{\omega} > 1$) regime. The scale length of the potential is close to the CL estimate $\Delta \sim 10 \lambda_{d0}$ is shorter than for case (a) because the average ion density in the Debye sheath is higher. This, in turn, is due to the absence of a magnetic presheath. Comparing the left and right panels, the signature of the magnetic presheath, at left, is a large drop in density in the quasi-neutral region. This density drop is given by the Boltzmann relation, and occurs in the oblique (but not the perpendicular) sheath case because the magnetic presheath must support a potential gradient in order to accelerate ions from $u_x \sim u_{\parallel} b_x \sim c_s b_x$ up to the Bohm condition $u_x \sim c_s$.

These variations in the width of the non-neutral sheath are of particular interest for rf considerations. First it is important to note that in the high-voltage (and hence strongly biased) case, most of the applied voltage drop occurs across the non-neutral sheath and not across the magnetic presheath. This is in contrast to the usual case of oblique thermal dc sheaths studied in the literature, where a large fraction of the total sheath voltage occurs in the quasi-neutral magnetic presheath.^{32,33} Second, in the capacitive limit (either perpendicular or strongly magnetized, and immobile) the width of the non-neutral sheath Δ determines the sheath capacitance. This is because the non-neutral sheath is devoid of electrons, which are the highly conducting species; consequently, in this limit the non-neutral sheath can be modeled as a vacuum gap capacitor.^{25,27,28} We will see that the tendency for the impedance to increase with Δ is a general feature of the present model that transcends the capacitive limit.

The ion dynamics in the mobile ion regime can sometimes be much richer than suggested by case (a) illustrated in Figs. 1 and 2. Indeed, for $\omega \sim \omega_{pi}$ locally in the non-neutral Debye sheath, (which implies $\hat{\omega} < 1$, but not too small) one might expect the possibility of exciting some variant of an ion plasma wave. An example is shown in Fig. 3 for the dimensionless parameters $\Omega=0.1$, $b_x=0.1$, $\omega=0.1$, $V_{pp}=11.25$, denoted case (c). The waves seen here have the

frequency of the driving voltage and a k -value that is measured and compared with a dispersion relation in Appendix B.

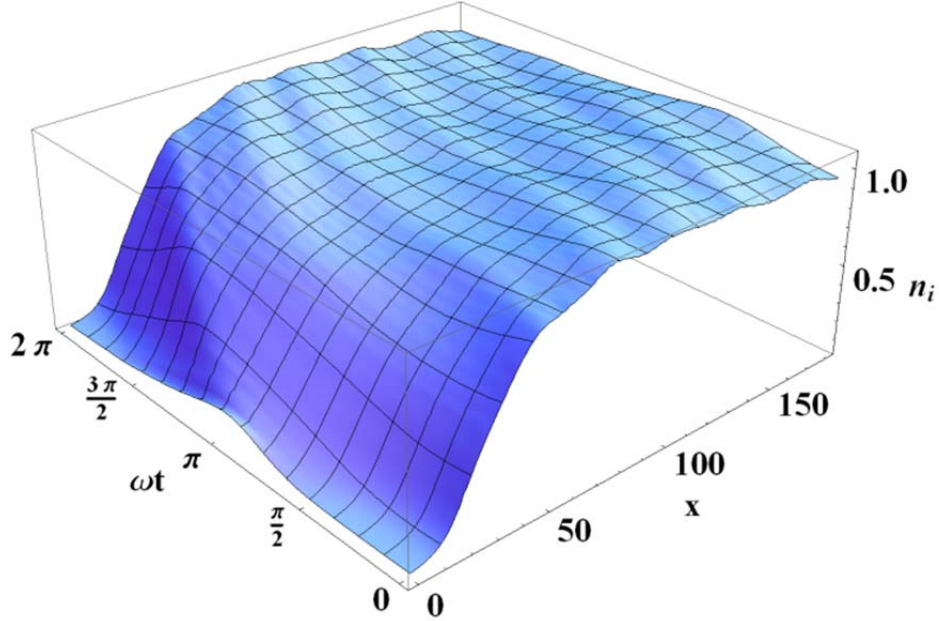


Fig. 3. Space-time plot of the ion density in dimensionless units for case (c): $\Omega=0.1$, $b_x=0.1$, $\omega=0.1$, $V_{pp}=11.25$. This more extreme limit of mobility and glancing angle exhibits a richer ion dynamics which includes the present of wave-like structures.

IV. RF properties of the sheath

In this section the rf properties of the sheath are considered with special attention to the sheath impedance and its role in deriving a sheath BC. As discussed in the introduction, it has proven to be very useful to describe the response of the sheath as a linear lumped circuit element with a characteristic impedance at the frequency of the applied rf wave. This description is necessarily approximate because of the nonlinear nature of an rf sheath when $eV \gg T$ but nevertheless useful and appropriate when the sheath impedance is used as a BC to couple the sheath physics to a linear global wave code. The approximations and justification are considered in the following. Throughout Sec. IV, voltages (V) and currents (J and I) refer to the rf components at frequency ω .

A. Sheath impedance

The effective impedance of a single sheath Z_s (here taken to be the sheath near the $x = 0$ wall) is defined as

$$V_{1\omega} - \Phi_{0\omega} = V_{1\omega} = I_{\omega} Z_S = J_{\omega} A Z_S \equiv J_{\omega} z, \quad (23)$$

where $V_{1\omega}$ is the change in rf voltage across the sheath, i.e. in the positive x direction [see Eq. (8)] and $I_{\omega} = J_{\omega} A$ is the rf current through the sheath, both at frequency ω . Henceforth in this section, the subscript ω will be dropped for notational simplicity. This impedance does not directly involve either the rectified potential or the contributions of the higher harmonics $2\omega, 3\omega, \dots$, which are small.^{40,41} Note that while the central potential Φ_0 has dc and 2ω components, its ω component vanishes by symmetry [see e.g. Fig. 1]. In Eq. (23), $z = AZ_S$ is an impedance parameter; the current density in the positive x direction is

$$J = J_i + J_e + J_d, \quad (24)$$

including the contributions of ions, electrons and displacement current; and A is the area of the sheath in the y - z plane. Equation (23) expresses a complex linear relationship between V_1 and I , which we apply to the (nonlinear) rf sheath to obtain an effective impedance at the driving rf frequency ω . This is done by projecting the in-phase and out-of-phase components of the current in Eq. (23). Let

$$J = \alpha V_1 + \beta \dot{V}_1, \quad (25)$$

where we define $\dot{V}_1 \equiv dV_1/dt$. Multiplying both sides by V_1 and time averaging over a cycle (denoted $\langle \dots \rangle$) gives $\langle J V_1 \rangle = \alpha \langle V_1^2 \rangle$; multiplying both sides by \dot{V}_1 and averaging gives $\langle J \dot{V}_1 \rangle = \beta \langle \dot{V}_1^2 \rangle$. Combining these relations with Eq. (25) gives the following voltage-current relation for the rf sheath

$$J = \frac{\langle J V_1 \rangle}{\langle V_1^2 \rangle} V_1 + \frac{\langle J \dot{V}_1 \rangle}{\langle \dot{V}_1^2 \rangle} \dot{V}_1 \quad (26)$$

Employing $\dot{V} = -i\omega V$ outside the time averages (the quantities inside the averages are to be computed from the nonlinear model of Secs. II and III which involve only real quantities), and using Eq. (23), we obtain the following expression for the impedance parameter z :

$$\frac{1}{z} = \frac{\langle J V_1 \rangle}{\langle V_1^2 \rangle} - \frac{i\omega \langle J \dot{V}_1 \rangle}{\langle \dot{V}_1^2 \rangle} \quad (27)$$

We take Eq. (27) to be the definition of the effective rf-sheath impedance.

It is useful to check the validity of this general result by considering the purely capacitive and purely resistive limits. For example, a capacitive response, typical for plasma processing

applications,^{28,42-44} would be given by $J = C' \dot{V}_1$ where $C' = C/A$ is the capacitance parameter. Substituting into Eq. (27), and using the identity $\langle V_1 \dot{V}_1 \rangle = 0$, yields $1/z = -i\omega C'$ or $Z_s = i/\omega C'$, the standard result for the capacitive limit. Similarly, for a resistive response, $J = V_1/(AR)$, Eq. (27) yields $Z_s = R$, where R is the resistance of the sheath. The capacitive limit of the sheath impedance occurs when the displacement current dominates the total current through the sheath, and the resistive limit occurs when the particle currents are the most important.

Because the rf sheath is inherently nonlinear, other definitions for z are possible, and in some limits may yield slightly different results. Recall that while the driving voltage V_1 is purely sinusoidal, the voltage $V_1 - \Phi_0$ across one sheath is not strictly sinusoidal, because Φ_0 contains 2ω and higher components arising from the oscillations of the central potential Φ_0 as evident from Fig. 1. These corrections were neglected in deriving Eq. (27). In some regimes, J contains a broad spectrum of frequencies which when multiplied by Φ_0 could contribute under the time-averages. Thus alternative, and not completely equivalent, expressions can be derived by using other projections to obtain the real and imaginary parts of z . Because the higher harmonics of the sheath response are small,^{40,41} we will not be overly concerned about such ambiguities, especially since we intend to apply the results of this study in rf codes which only simulate the linear rf wave physics at a single frequency. Particle-in-cell simulations⁴³ have recently confirmed the accuracy of the linear lumped circuit approach to sheath modeling in the capacitive limit. It should be emphasized that the linear impedance approximation is made only in the present section; the sheath model in Secs. II and III retains the full nonlinearity of the problem.

Finally, as is well known, charge conservation from Maxwell's equations can be expressed as $\nabla \cdot \mathbf{J} = 0$ where $\mathbf{J} = J_x \mathbf{e}_x$, is the *total* current given by Eq. (24), i.e. including the displacement current. Consequently, the impedance defined here is independent of where the current is evaluated, since $J_x = \text{constant}$ across the sheath. It will be convenient later to evaluate J_x at the wall. Conceptually, the sheath BC should be thought of as applying at the entrance to the magnetic presheath, since the macroscopic models, which the sheath BC will be used in, cease to be valid in both the magnetic presheath and sheath regions.

B. Effective sheath width

For future use, we also define an effective sheath width Δ_{eff} , useful in the capacitive sheath limit, where the dominant response is from the displacement current. For a (single) vacuum gap of width Δ_{eff} we have

$$C' = \frac{1}{4\pi\Delta_{\text{eff}}} , \quad (28)$$

hence by Eq. (27) we have

$$\Delta_{\text{eff}} = \frac{\langle \dot{V}_1^2 \rangle}{\langle 4\pi J \dot{V}_1 \rangle}. \quad (29)$$

This result is useful for comparing our code results against the Child-Langmuir scaling in the capacitive limit, given by

$$\Delta_{\text{CL}} = \lambda_{d0} \left(\frac{e \langle \Phi_0 \rangle}{T_e} \right)^{3/4} \quad (30)$$

where λ_{d0} is the reference Debye length and $\langle \Phi_0 \rangle$ is the rectified (i.e. time-averaged) sheath potential ($\langle \Phi_0 \rangle \propto V_1$). In the CL model, the sheath impedance is purely capacitive and given by Eq. (28) employing Δ_{CL} for Δ_{eff} .

C. Generalized sheath boundary condition

One approach to quantitatively calculating the rf wave fields and their associated sheath potential at the boundary is to use an rf sheath BC.^{25,27} It is straightforward to derive a BC that treats the sheath as a thin vacuum region and includes the effect of its capacitance. This approach has been adopted in a number of global wave codes.^{13,14,18-20}

One problem with the work done to date is that the resistive impedance has been neglected. This could influence both the strength of the wave-fields at the surface and the sheath power dissipation (e.g. hot spots and reduced heating efficiency). In this section, we address the question of how to generalize the rf sheath BC to use the full complex impedance z derived here.

To treat the sheath self consistently and satisfy Maxwell's equations, rf wave propagation codes need a relation between \mathbf{E}_t and D_n on the plasma side of the sheath. Here, the subscripts "n" and "t" denote the directions "normal" and "tangential" to the sheath-plasma interface. We obtain this relation from the present calculation noting that \mathbf{E}_t is related to the sheath voltage V_{sh} and D_n is related to the sheath current J . For \mathbf{E}_t we have

$$\mathbf{E}_t = -\nabla_t V_{\text{sh}} = \nabla_t V_1 = \nabla_t (Jz) \quad (31)$$

(Most rf codes have the convention that the wall is at ground and the sheath voltage V_{sh} is measured in the plasma at the sheath entrance. However, in the sheath model described in Sec. II, the plates are oscillating at potential V_1 , so there is a sign change in going from V_{sh} to V_1 .) Here, $J = J_n$ is related to D_n by

$$D_n = \frac{4\pi i}{\omega} J_n. \quad (32)$$

From these expressions we have the final result, to be employed as the new sheath BC in rf codes:

$$\mathbf{E}_t = \nabla_t(J_n z) = \nabla_t \left(\frac{\omega}{4\pi i} D_n z \right), \quad (33)$$

which is evaluated on the plasma side of the sheath-plasma interface. Equation (33) is a straightforward but important result for future applications: together with a characterization of z , it provides the desired generalization of the sheath BC.

Note that in the capacitive limit, using $1/z = -i\omega C'$ and Eq. (28) we recover the original form of the rf sheath BC,²⁷ which was derived retaining only the capacitive impedance, viz.

$$\mathbf{E}_t = \nabla_t(\Delta_{\text{eff}} D_n). \quad (34)$$

Note also that in the limit $\Delta_{\text{eff}} \rightarrow 0$ or $z \rightarrow 0$ both forms recover the usual conducting wall BC, $\mathbf{E}_t = 0$.

To summarize this section, Eqs. (27) and (33) combine to give the rf sheath BC including both the capacitive and the resistive impedance. To evaluate z in the general case, one must first calculate the function $J(t)$, given $V_1(t)$ by solving the sheath equations discussed in Sec. II. This model generalizes our previous work to include the effects of ion mobility, ion magnetization and arbitrary magnetic field angle with respect to the sheath.

D. Sheath power dissipation

In the tokamak SOL rf sheaths form on the antenna, wall and limiters. As discussed in the introduction, this contributes to reduced heating efficiency, hot spots on the antenna and near-by limiters, and enhanced sputtering, SOL electric fields and plasma convection.⁴⁻¹³ In addition to modeling the sputtering energies available to ions that have been accelerated through the sheath, an important application of the rf sheath model is to understand power dissipation.

There are at least two contributions to the power flux on the plates. One is the particle energy that must be supplied by the plasma sources at the midplane $x = L = (x_1 + x_2)/2$ to (i) emit cold ions at or above the sound speed parallel to the magnetic field, and (ii) maintain a Maxwellian electron distribution at temperature T in the presence of the electron heat flux to the wall due to tail electron losses. These source contributions will not be considered here, but were treated in the immobile ion limit in the appendix of Ref. 45. The other energy source in the present model is the dissipation of rf power in the sheath. This electrical power is supplied by the rf wave and is given by

$$P = A \langle JV_1 \rangle \quad (35)$$

where J and V_1 are the total rf current and voltage across the sheath, with the former given by Eq. (24). The quantity $\langle JV_1 \rangle$ can be calculated from the full nonlinear model without further approximation. Comparing with Eq. (27) this calculation may also be expressed in terms of our definition of impedance as

$$P = A \langle V_1^2 \rangle \operatorname{Re} \left(\frac{1}{z} \right) \quad (36)$$

We will see that z is a nonlinear (and typically increasing) function of $|V_1|$, so that P will scale more slowly than $\langle V_1^2 \rangle$ particularly when $|eV_1/T|$ is large.

Numerical results for z will be presented in Sec. V; however, to understand the meaning of Eq. (35), it is instructive to recall the calculation of the power in the immobile ion limit.⁴⁵ In this limit the ion current at frequency ω is negligible in Eq. (35) and the displacement current is out of phase with V_1 . Only the electron current at the plate from Eq. (11) contributes and results in

$$P = \frac{A v_e T}{(2\pi)^{1/2}} b_x n_0 \langle V_1 \exp[e(V_1 - \Phi_0)/T] \rangle \quad (37)$$

Approximating $\Phi_0 \approx \langle \Phi_0 \rangle$ and employing Eq. (8) as well as standard Bessel function identities, the result is

$$P = \frac{A v_e T}{(2\pi)^{1/2}} b_x n_0 e^{-e\langle \Phi_0 \rangle/T} \xi I_1(\xi) \quad (38)$$

where $\xi = eV_{pp}/(2T)$. The time-averaged electron particle flux at the plate is almost the same integral, i.e. $\Gamma = -A \langle J \rangle / e$ and takes the form

$$\Gamma = \frac{v_e}{(2\pi)^{1/2}} b_x n_0 e^{-e\langle \Phi_0 \rangle/T} I_0(\xi) \quad (39)$$

Thus the power can be expressed as

$$P = A \Gamma T \xi I_1(\xi) / I_0(\xi) \quad (40)$$

In the high voltage limit, $\xi \gg 1$, using the asymptotic forms of $I_0(\xi)$ and $I_1(\xi)$ which are identical to leading order, we finally have

$$P \sim A n_0 u_{x0} T \xi \sim A n_0 b_x c_s e V_{pp} / 2 \quad (41)$$

where, from ambipolarity, $\Gamma = \Gamma_e = \Gamma_i = n_0 u_{x0} \sim n_0 b_x c_s$. The final result may be interpreted in terms of the energy that the ions gain in falling down the dc sheath potential as they strike the wall.⁴⁵ (Note that Ref. 45 employs the notation $A_n = Ab_x$ where A_n is the projection of the plate area normal to the magnetic field.) Thus the present impedance formalism includes this effect in the immobile ion limit.

RF energy that is dissipated in the sheath through Eq. (36) must ultimately come from the wave that is driving the sheath. Appendix C illustrates how this comes about by demonstrating energy conservation between the waves and sheath when the impedance matching sheath BC is employed.

V. Sheath impedance results

Numerical results for the sheath impedance defined by Eq. (27) are given in Table 1. Throughout this section, results are presented in terms of the dimensionless quantities defined in Eq. (21). The table shows eight cases, identified by labels (a) through (g) which sample important variations in the input parameters $\hat{\Omega}$, $\hat{\omega}$ and b_x . The real and imaginary normalized impedance values (\hat{z}_r and \hat{z}_i) shown here are all calculated for $\hat{V}_{pp} = 10$. Note that $\hat{\Omega}$ is irrelevant for perpendicular sheaths ($b_x = 1$).

Table I. Characterization of sheath impedance for a range of parameters.

$\hat{\Omega}$	$\hat{\omega}$	b_x	\hat{z}_r	\hat{z}_i	case
0.1	0.3	0.2	7.92	6.19	a
0.1	0.3	0.1	11.37	10.83	b
0.1	0.1	0.1	22.57	4.77	c
-	0.001	1.0	3.63	0.01	d
-	3.0	1.0	0.41	1.08	e'
-	9.0	1.0	0.05	0.43	e
0.1	3.0	0.2	0.22	2.08	f
1.0	3.0	0.2	0.10	1.49	g

At large angles the impedance is mostly real (resistive) for low frequencies, i.e. $\omega/\omega_{pi} \ll 1$, and imaginary (capacitive) for high frequencies. The cross-over point where the resistive and capacitive parts are comparable occurs at $\omega/\omega_{pi} \sim 3$ (case e'). The same trends are true at small angles, except the cross-over point occurs at smaller $\omega/\omega_{pi} \sim 0.3$ (case b). Note that the absolute value of the impedance $|\hat{z}|$ becomes very large when all three control parameters $\hat{\Omega}$, $\hat{\omega}$ and b_x

are small (cases a, b, c) and conversely $|\hat{z}|$ becomes very small when $\hat{\Omega}, \hat{\omega}$ and b_x are large (case e).

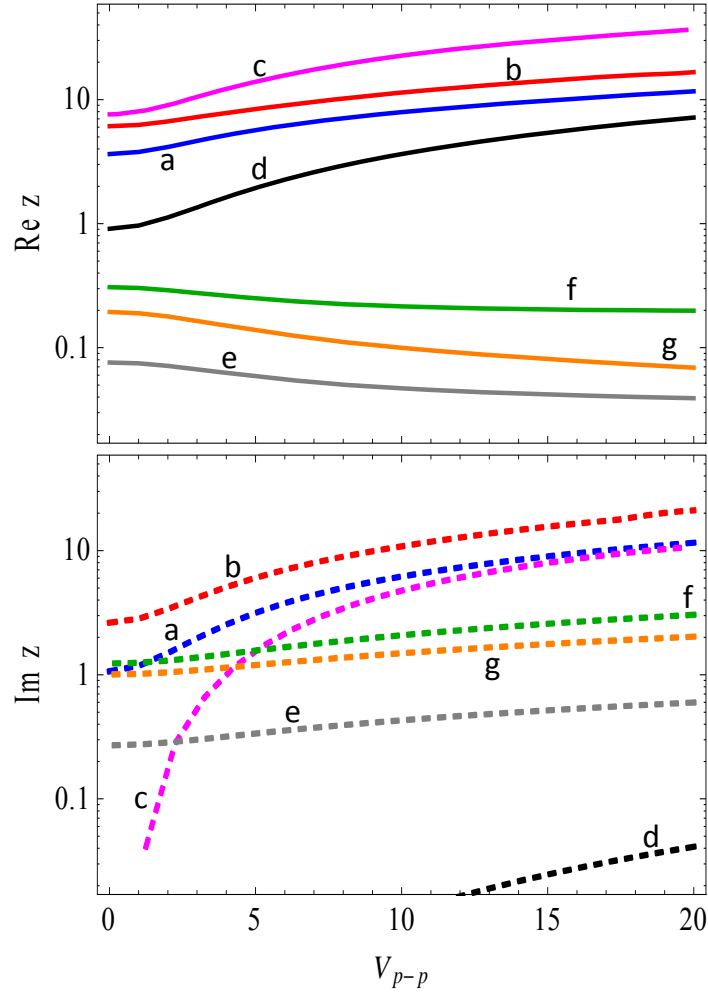


Fig. 4. Dimensionless impedance \hat{z} vs. driving voltage \hat{V}_{pp} for cases identified in Table I: upper panel \hat{z}_r , lower panel \hat{z}_i .

Figure 4 shows the variation of impedance with the driving voltage. Note that $|\hat{z}|$ is a generally increasing function of \hat{V}_{pp} and that as expected \hat{z} tends to a constant value as $\hat{V}_{pp} \rightarrow 0$, since in that limit the problem is strictly linear. Cases (a) and (b) show the effect of the angle (i.e. b_x) on a marginally mobile sheath (see Table 1 for parameters): impedance rises as the angle decreases. This result may be understood in terms of the effect of the magnetic presheath on the local density in the non-neutral sheath, which then reduces the electron current and increases the impedance. The argument is that the magnetic presheath must accelerate ions from their velocity $u_{x0} \sim c_s b_x$ at the source (at $x = L$) to a velocity of order $u_x \sim c_s$ at the entrance to the non-neutral sheath. For smaller b_x greater acceleration is required which implies a larger change in Φ in the

magnetic presheath. From the Boltzmann electron relation, Eq. (2) this means a lower density in non-neutral sheath. Alternatively, from the average of Eq. (3), $n_{i1}/n_0 \sim u_{x0}/c_s \sim b_x$ where n_{i1} is the ion density at the entrance to the non-neutral sheath.

Cases (b) and (c) in Fig. 4 show the effect of mobility on a small angle sheath: the small $\hat{\omega}$ results in a large resistive impedance. The particle currents have more time to cross the sheath. (Comparing λ_d with the distance ions travel at speed c_s in a wave period gives the mobility parameter ω/ω_{pi}). Two more extreme cases of mobility are compared with cases (a) and (f) which illustrate the (partially) resistive and capacitive limits as $\hat{\omega}$ changes with other parameters fixed. A similar comparison is made with cases (d) and (e) but this time for perpendicular sheaths (hence no magnetic presheath effects) and more extreme values of $\hat{\omega}$.

Finally, cases (f, $\hat{\Omega} = 0.1$) and (g, $\hat{\Omega} = 1$) show the effect of magnetization on the sheath in the immobile ion limit: the impedance remains mostly capacitive for all $\hat{\Omega}$. [We say for all $\hat{\Omega}$ because the immobile strongly magnetized case $\hat{\Omega} \gg 1$ is already known to be capacitive.²⁷ This previous finding is also verified in case (e, $b_x=1$) since a perpendicular sheath is isomorphic to $\hat{\Omega} \gg 1$, i.e. the ions remain tied to field lines and there is no magnetic presheath.] Thus ion mobility turns out to play a very significant role. When $\omega > \omega_{pi}$ the capacitive sheath approximation is expected to be applicable, even when $\Omega < \omega_{pi}$, i.e. $\rho_s > \lambda_d$, and a magnetic presheath forms. This is discussed further in connection with Fig. 5.

Figure 5 shows the voltage variations of some capacitive sheaths in the immobile limit. The upper panels verify that $\hat{z}_i \gg \hat{z}_r$ for all cases. Therefore, these are cases for which the results may be meaningfully described in terms of an effective sheath width (vacuum capacitor gap), Eq. (29), and with the expressions resulting from the CL law, Eq. (30).

The lower left panel shows that $\hat{\Delta}_{CL}$ is an excellent approximation to the more general $\hat{\Delta}_{eff}$ calculated here for perpendicular (or equivalently, strongly magnetized $\Omega \gg \omega_{pi}$) immobile ion sheaths. This is the limit for which the sheath BC was originally derived. The same comparison is made for cases (f) and (g) in the lower right panel. These cases have magnetic presheaths and are not as strongly magnetized. The CL law gives the correct qualitative trend in all cases, but is quantitatively inaccurate in case (f) where the sheath is weakly magnetized.

One reason for this again traces back to the effect of the magnetic presheath on the local density in the non-neutral sheath. For reasons explained previously the magnetic presheath induces a density drop in the non-neutral sheath. This increases the local λ_d and therefore Δ_{eff} is larger than Δ_{CL} which, in Eq. (30), is based on the reference Debye length λ_{d0} . The mismatch is worse when $\hat{\Omega}$ is small, the regime where the magnetic presheath plays the most important role.

For completeness, we close this section with an examination of the ‘‘rectified’’ voltage $V_{rect} \equiv \langle \Phi_0 \rangle$ predicted by the present model. Results are given in Fig. 6. These results show remarkably little sensitivity to parameters and reinforce the statement made earlier that most of

the voltage drop in high voltage cases occurs in the non-neutral sheath, which simply rectifies a nearly constant fraction of the applied rf voltage. This voltage adds to the $3T_e$ thermal sheath.

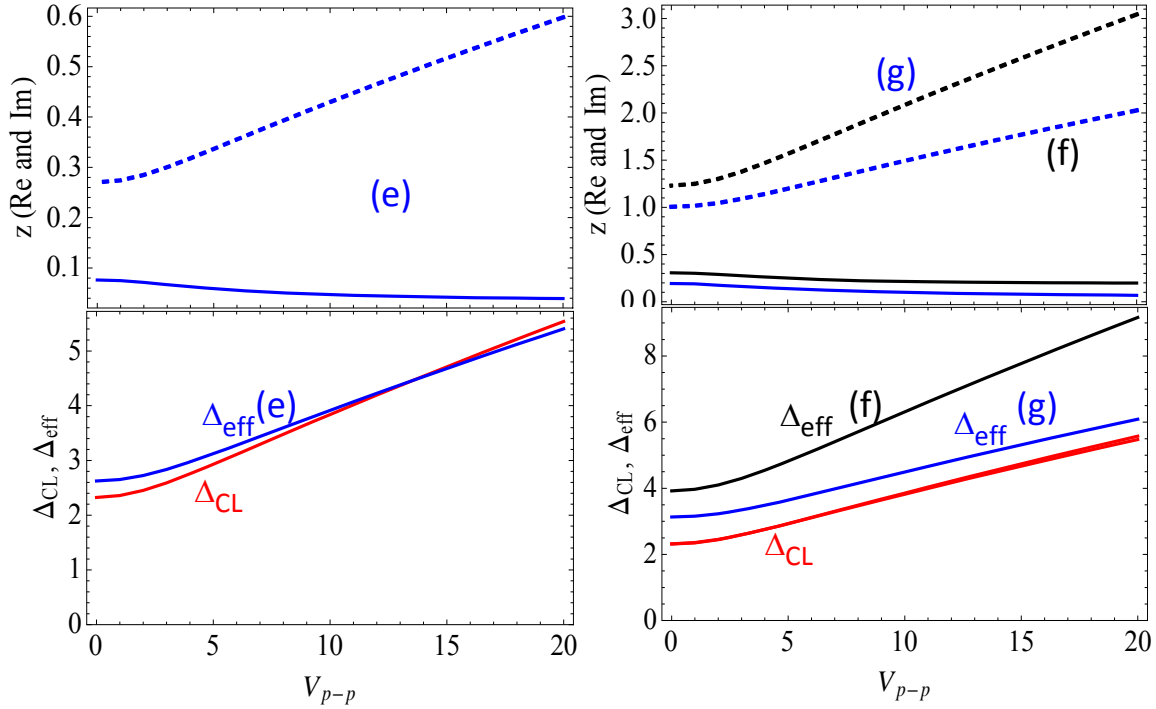


Fig. 5. Voltage variation of dimensionless impedance \hat{z} (upper panels) and dimensionless sheath width (lower panels) for several cases that are marginally in the immobile limit and hence show a mostly capacitive response, \hat{z}_i (dashed) \gg \hat{z}_r (solid). The left panels are for case (e), the perpendicular immobile limit. The right panels show cases (g, blue) and (f, black). Various measures of the sheath width, $\hat{\Delta}_{eff}$ and $\hat{\Delta}_{CL}$, are explained in the main text. For cases (f) and (g) the $\hat{\Delta}_{CL}$ curves (red) lie on top of each other.

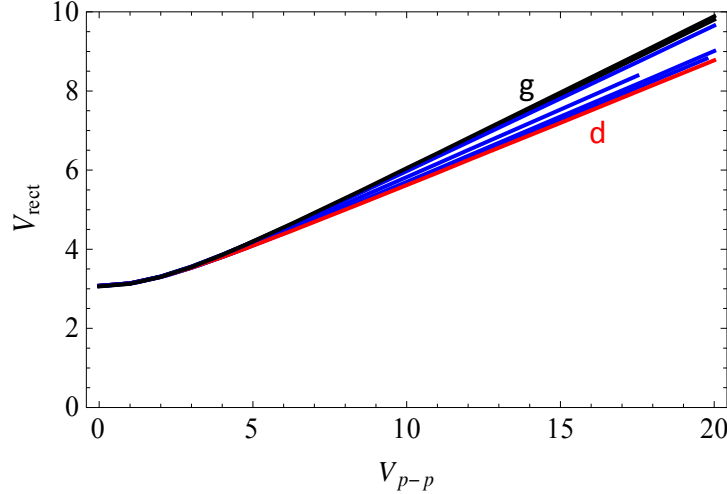


Fig. 6. Rectified voltage (including the thermal sheath contribution) for all the cases in Table I, superimposed. The highest curve is case (g), one of the most immobile, closely followed by case (e), both are shown in black. The lowest curve is case (d), the most mobile, shown in red.

VI. Summary and conclusions

In this paper we have described a time-dependent one-dimensional cold-ion fluid model with Maxwell-Boltzmann electrons for describing rf sheaths in an oblique magnetic field. The model reproduces well known results for the angular and magnetic field dependence of dc sheaths and also reproduces previous results for rf sheaths in the strongly magnetized immobile ion limit (i.e. $\omega, \Omega \gg \omega_{pi}$). In particular, the model places the often-employed Child-Langmuir scaling of sheath capacitance on a solid footing in that limit (see Fig. 5).

The rf sheath model was then employed to derive an effective sheath impedance which relates the rf current flowing through the sheath to the rf voltage that is driven across the sheath. The effective impedance was numerically calculated in a variety of parameter regimes (Table I and Fig. 4). In general it was found that the impedance develops a strong resistive contribution in the mobile ion limit $\omega/\omega_{pi} \ll 1$ and conversely is mostly capacitive in the immobile ion limit $\omega/\omega_{pi} \gg 1$; both the real and imaginary parts of the impedance usually decrease with magnetization Ω/ω_{pi} ; and the magnitude of the impedance generally increases with rf voltage and decreases with the magnetic field angle, i.e. with b_x . These changes can be attributed in part to the importance of particle currents (relative to displacement currents) at smaller values of ω/ω_{pi} and partly to the role of the magnetic presheath on the density (at the entrance to the non-neutral sheath) at small values of b_x and Ω/ω_{pi} .

Rectification is insensitive to parameters (Fig. 6) and for large applied rf voltages ($eV_{pp} \gg T$) most of the voltage drop occurs across the non-neutral Debye sheath.

The main results of our paper are to be found in the definition of effective impedance, Eq. (27), its application in a generalized sheath boundary condition Eq. (33), and the numerical scaling of the impedance (Table I and Fig. 4). It is anticipated that the main application of this work will be to use the generalized sheath boundary condition in global wave codes in order to model sheath effects without having to resolve the sheath region itself. To make this goal practical, future work will concentrate on developing analytical or numerical fits for the impedance $\hat{z}(\hat{\omega}, \hat{\Omega}, b_x, \hat{V}_{pp})$ that can easily be implemented in global full-wave codes. In addition, future work will be required to characterize regimes for which the Maxwell-Boltzmann approximation for the electrons is inadequate, i.e. where the inequality mentioned just before Eq. (1) is violated. High voltage broad sheaths at low frequencies, and cases where b_x is very small will require special attention.

Acknowledgements

This material is based upon work supported by the U.S. Department of Energy Office of Science, Office of Fusion Energy Sciences under Award Number DE-FG02-97ER54392.

Appendix A: Dimensionless Equations

The sheath equations can be cast into dimensionless form by normalizing time to ω_{pi0}^{-1} and distance to the Debye length, $\lambda_{d0} = (T_e / 4\pi n_0 e^2)^{1/2}$, which is the natural scale length of a sheath. The complete set of dimensionless variables is

$$\begin{aligned} \hat{L} &= L / \lambda_{d0}, \quad \hat{t} = \omega_{pi0} t, \quad \hat{u} = u / c_s, \quad \hat{n} = n / n_0, \quad \hat{J} = J / (n_0 e c_s), \\ \hat{V} &= eV / T_e, \quad \hat{\Phi} = e\Phi / T_e, \quad \hat{z} = z \omega_{pi0} / (4\pi \lambda_{d0}) \end{aligned} \quad (\text{A1})$$

Here n_0 is the density upstream of the sheath (at the symmetry plane), T_e is the (constant) electron temperature, $c_s = (T_e / m_i)^{1/2}$ and z is the sheath impedance parameter ($z = A Z_s$). Taking the charge state to be $Z = 1$, the dimensionless equations obtained from Eqs. (1) – (6) and (8) – (11), (20) are

$$\frac{\partial^2 \hat{\Phi}}{\partial \hat{x}^2} = -(\hat{n}_i - \hat{n}_e) \quad (\text{A2})$$

$$\hat{n}_e = \exp(\hat{\Phi} - \hat{\Phi}_0) \quad (\text{A3})$$

$$\frac{\partial \hat{n}_i}{\partial \hat{t}} + \frac{\partial}{\partial \hat{x}} (\hat{n}_i \hat{u}_x) = 0 \quad (\text{A4})$$

$$\left(\frac{\partial}{\partial \hat{t}} + \hat{u}_x \frac{\partial}{\partial \hat{x}} \right) \hat{u}_x = -\frac{\partial \hat{\Phi}}{\partial \hat{x}} + \hat{\Omega} \hat{u}_p \quad (\text{A5})$$

$$\left(\frac{\partial}{\partial \hat{t}} + \hat{u}_x \frac{\partial}{\partial \hat{x}} \right) \hat{u}_p = \hat{\Omega} \hat{u}_\parallel b_x - \hat{\Omega} \hat{u}_x \quad (\text{A6})$$

$$\left(\frac{\partial}{\partial \hat{t}} + \hat{u}_x \frac{\partial}{\partial \hat{x}} \right) \hat{u}_\parallel = -\frac{\partial \hat{\Phi}}{\partial \hat{x}} b_x \quad (\text{A7})$$

$$\hat{n}_{i1} \hat{u}_{x1} + \mu b_x \exp(\hat{V}_1 - \hat{\Phi}_0) - \frac{\partial^2 \hat{\Phi}_1}{\partial \hat{t} \partial \hat{x}} + [\omega t \rightarrow \omega t + \pi] = 0 \quad (\text{A8})$$

$$\hat{u}_{x0} + \mu b_x \langle \exp(\hat{V}_1 - \hat{\Phi}_0) \rangle = 0 \quad (\text{A9})$$

where for convenience, we define

$$\mu = \frac{\hat{v}_e}{(2\pi)^{1/2}} = \frac{1}{(2\pi)^{1/2}} \left(\frac{m_i}{m_e} \right)^{1/2} \quad (\text{A10})$$

Dropping the carats, the main results of Sec. IV are given in dimensionless form by

$$\Delta_{\text{eff}} = \frac{\langle \dot{V}_1^2 \rangle}{\langle J \dot{V}_1 \rangle}, \quad (\text{A11})$$

and

$$\frac{1}{z} = \frac{\langle J V_1 \rangle}{\langle V_1^2 \rangle} - \frac{i\omega \langle J \dot{V}_1 \rangle}{\langle \dot{V}_1^2 \rangle}, \quad (\text{A12})$$

where the expression for the sheath width [Eq. (A11)] is only applicable in the capacitive limit, $Z_s \rightarrow i/(\omega C)$, but the expression for the impedance z [Eq. (A12)] is valid generally, i.e. in both the resistive and capacitive limits.

Finally, the derivations in this paper are in Gaussian units, e.g. Eqs. (1) – (11) while the numerical results are presented in dimensionless form. To convert the dimensionless impedance

to a dimensional impedance in SI (Système International) units we note that Eq. (23), $V = IZ_s$ holds in both Gaussian and SI units. Then it follows from Eq. (A1) that the impedance in ohms is given by

$$Z_s(\Omega) = 9 \times 10^{11} \frac{4\pi\lambda_{d0}(\text{cm})}{\omega_{pi0}(\text{s}^{-1})A(\text{cm}^2)} \hat{z}. \quad (\text{A13})$$

Appendix B: Sheath-driven waves analysis

In order to better understand the wave-type behavior seen in Fig. 3, a linear analysis of a model problem is described in this appendix. From the model, a dispersion relation can be derived and compared with the waves obtained for that case.

From the full nonlinear model of Sec. II, we consider a region far upstream for which it is reasonable to assume an equilibrium that is independent of space and time. Specifically we take

$$n_i = n_e = n_0 = \text{const}, \quad (\text{B1})$$

$$\Phi = \Phi_0, \quad (\text{B2})$$

$$v_0 = u_p = u_{||} = u_x = 0. \quad (\text{B3})$$

The neglect of background flow is approximate, but sufficient for present purposes. Linearizing the equations about this equilibrium and combining them results in the dimensionless dispersion relation

$$\omega^2(\omega^2 - \Omega^2)(1 + k^2) = k^2(\omega^2 - \Omega^2 b_x^2) \quad (\text{B4})$$

which may be solved for k as a function of ω . Results for the parameters of case (c) in Fig. 3, viz. $\Omega=0.1$, $b_x=0.1$ are shown in Fig. 7. At the driving frequency $\omega = 0.1$ there is a long wavelength mode with $k \ll 1$.

In order to compare this with the numerical model, case (c) was computed again using a large numerical box size L to display the upstream waves more clearly. Then, the density perturbation was separated from the background density. The result is shown in Fig. 8.

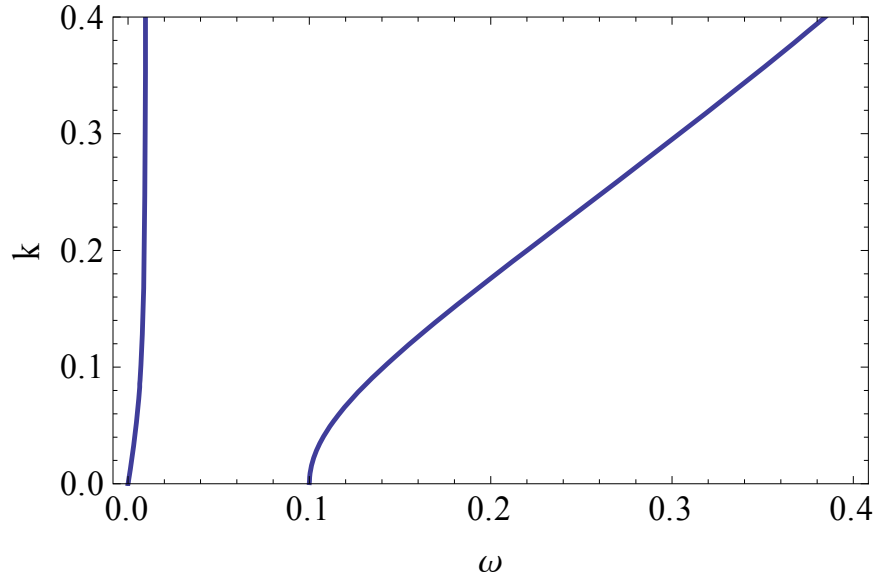


Fig. 7. Dispersion relation for the analytic wave model using the parameters of case (c) in terms of dimensionless parameters.

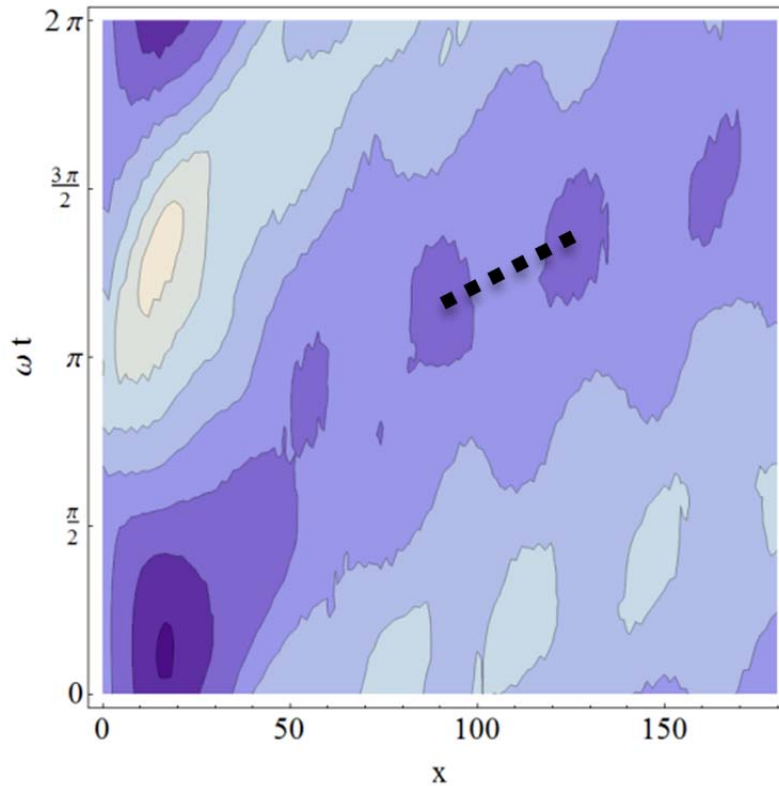


Fig. 8. Shaded contour plot of $\delta n = n - \langle n \rangle_t$ where $\langle n \rangle_t(x)$ is the time-averaged ion density profile. The case is the same as shown in Fig. 3, viz. case (c). The dashed line is used to determine the phase velocity and k-value for this wave.

Note the wave structure which appears to be born in the non-neutral sheath region near $x = 20$ and propagates outward in x . The wave repeats itself at the two $(x, \varphi = \omega t)$ locations indicated by the ends of the dashed line in Fig. 8. Their difference may be used to calculate a wavenumber and phase velocity. We estimate $k = \Delta\varphi/\Delta x = 0.020$ and a phase velocity $\omega/k = 4.9$, much larger than the local sound speed. The model dispersion relation gives a phase velocity which grows from order unity (i.e. of the order of the sound speed) for $\omega > \Omega$ to infinity at $\omega = \Omega$, in qualitative agreement with the observations. The measured k value of 0.02 is also in qualitative agreement with the dispersion relation in so far as the dispersion relation predicts the existence of a long wavelength mode, $k \ll 1$ at $\omega = 0.1$.

Appendix C: Energy conservation

In this appendix, we consider the question of how a propagating rf wave provides the power to drive dissipative losses in the sheath. It is shown explicitly for a simple example that the rf sheath boundary condition has the proper energy conservation properties.

We consider the very simplest case of an electromagnetic SW propagating parallel to $\mathbf{B} = B_0 \mathbf{e}_z$ where the B-field is aligned with the normal to the sheath surface. (Note that the coordinate system in this appendix is different from that used in the main text.) The Poynting flux of the wave is

$$S_z = \frac{c}{16\pi} E_x^* B_y + cc, \quad (C1)$$

Using the Maxwell equations $\mathbf{n} \times \mathbf{B} = -\mathbf{D}$ and $\mathbf{n} \times \mathbf{E} = \mathbf{B}$ where $\mathbf{n} = \mathbf{k}c/\omega$ and \mathbf{D} is the displacement vector, taking $k_y = 0$ and the non-zero SW polarization components E_x, E_z, B_y we have $n_x B_y = -D_z$. Thus the Poynting flux becomes

$$S_z = -\frac{\omega}{16\pi k_x} E_x^* D_z + cc. \quad (C2)$$

Next, consider the sheath BC. Applying Eq. (33) in this geometry yields

$$E_x = \frac{\omega k_x A Z}{4\pi} D_z = ik_x Z A J_z = ik_x Z I. \quad (C3)$$

where $I = J_z A$ is the sheath current. The power dissipation in the sheath is

$$P = \langle I^2 Z \rangle = \frac{E_x^* I}{4ik_x} + cc. \quad (C4)$$

Then using $I = AJ_z = A\omega D_z/(4\pi i)$ and comparing with Eq. (C2) one immediately sees that

$$P = AS_z \quad (C5)$$

This shows that Poynting flux of the wave provides the power that is dissipated in the sheath.

As usual, when the wave impedance does not match the sheath impedance, a portion of the waves will reflect from the sheath surface, thereby reducing both the net Poynting flux and the sheath power losses. These effects are included automatically when the sheath BC is employed in a global wave code. The condition of impedance matching of the wave to the sheath is related to the excitation of the sheath plasma resonance,²⁹⁻³¹ which can result in very high voltage sheaths.¹⁸

References

- ¹ J.-M. Noterdaeme and G. Van Oost, *Plasma Phys. Control. Fusion* **35**, 1481 (1993).
- ² J.R. Myra, D.A. D'Ippolito, D.A. Russell, L.A. Berry, E.F. Jaeger and M.D. Carter, *Nucl. Fusion* **46** S455 (2006).
- ³ D. A. D'Ippolito and J. R. Myra, *J. Nucl. Mater.* **415**, S1001- S1004 (2011).
- ⁴ S. J. Wukitch, M. L. Garrett, R. Ochoukov, J. L. Terry, A. Hubbard, B. Labombard, C. Lau, Y. Lin, B. Lipschultz, D. Miller, M. L. Reinke, D. Whyte, and Alcator C-Mod Team, *Phys. Plasmas* **20**, 056117 (2013).
- ⁵ V. Bobkov, M. Balden, R. Bilato, F. Braun, R. Dux, A. Herrmann, H. Faugel, H. Fünfgelder, L. Giannone, A. Kallenbach, H. Maier, H.W. Müller, R. Neu, J.-M. Noterdaeme, Th. Pütterich, V. Rohde, N. Tsujii, F. Zeus, H. Zohm and the ASDEX Upgrade Team, *Nucl. Fusion* **53**, 093018 (2013).
- ⁶ J. Jacquot, D. Milanesio, L. Colas, Y. Corre, M. Goniche, J. Gunn, S. Heuraux, and M. Kubič, *Phys. Plasmas* **21**, 061509 (2014).
- ⁷ C. M. Qin, Y. P. Zhao, H. Q. Wang, X. J. Zhang, B. N. Wan, J.-M. Noterdaeme, F. Braun, V. Bobkov, H. Kasahara, E. H. Kong, L. Wang, Y. Shuai, Z. X. He, B. J. Ding, ICRF Team and EAST Team, *Plasma Phys. Control. Fusion* **55**, 015004 (2013).
- ⁸ Y. Corre, M. Firdaouss, L. Colas, A. Argouarch, D. Guilhem, J. Gunn, C Hamlyn-Harris, J. Jacquot, M. Kubic, X. Litaudon, M. Missirlian, M. Richou, G. Ritz, D. Serret and K. Vulliez, *Nucl. Fusion* **52**, 103010 (2012).
- ⁹ I. Cziegler, J. L. Terry, S. J. Wukitch, M. L. Garrett, C. Lau and Y. Lin, *Plasma Phys. Control. Fusion* **54**, 105019 (2012).
- ¹⁰ R.J. Perkins, J.-W. Ahn, R.E. Bell, A. Diallo, S. Gerhardt, T.K. Gray, D.L. Green, E.F. Jaeger, J.C. Hosea, M.A. Jaworski, B.P. LeBlanc, G.J. Kramer, A. McLean, R. Maingi, C.K. Phillips, M. Podesta, L. Roquemore, P.M. Ryan, S. Sabbagh, F. Scotti, G. Taylor and J.R. Wilson, *Nucl. Fusion* **53**, 083025 (2013).
- ¹¹ R. Ochoukov, D. G. Whyte, D. Brunner, D. A. D'Ippolito, B. LaBombard, B. Lipschultz, J. R. Myra, J. L. Terry and S. J. Wukitch, *Plasma Phys. Control. Fusion* **56**, 015004 (2014).
- ¹² P. Jacquet, L. Colas, M.-L. Mayoral, G. Arnoux, V. Bobkov, M. Brix, P. Coad, A. Czarnecka, D. Dodt, F. Durodie, A. Ekedahl, D. Frigione, M. Fursdon, E. Gauthier, M. Goniche, M. Graham, E. Joffrin, A. Korotkov, E. Lerche, J. Mailloux, I. Monakhov, C. Noble, J. Ongena, V. Petržilka, C. Portafaix, F. Rimini, A. Sirinelli, V. Riccardo, Z. Vizvary, A. Widdowson, K.-D. Zastrow, and JET EFDA Contributors, *Nucl. Fusion* **51**, 103018 (2011).
- ¹³ L. Colas, J. Jacquot, S. Heuraux, E. Faudot, K. Crombé, V. Kyrlytsya, J. Hillairet and M. Goniche, *Phys. Plasmas* **19**, 092505 (2012).
- ¹⁴ D. N. Smithe, D. A. D'Ippolito, and J. R. Myra, *AIP Conference Proceedings* **1580**, 89 (2014).
- ¹⁵ N. Bertelli, E.F. Jaeger, J.C. Hosea, C.K. Phillips, L. Berry, S.P. Gerhardt, D. Green, B. LeBlanc, R.J. Perkins, P.M. Ryan, G. Taylor, E.J. Valeo and J.R. Wilson, *Nucl. Fusion* **54**, 083004 (2014).
- ¹⁶ D. Van Eester, K. Crombé and V. Kyrlytsya, *Plasma Phys. Control. Fusion* **55**, 055001 (2013).

- ¹⁷ J.R. Myra and D.A. D'Ippolito, *Plasma Phys. Controlled Fusion* **52**, 015003 (2010).
- ¹⁸ H. Kohno, J. R. Myra, and D. A. D'Ippolito, *Phys. Plasmas* **19**, 012508 (2012).
- ¹⁹ D. A. D'Ippolito, J. R. Myra, R. Ochoukov, and D. G. Whyte, *Plasma Phys. Control. Fusion* **55**, 085001 (2013).
- ²⁰ H. Kohno, J. R. Myra, and D. A. D'Ippolito, *Phys. Plasmas* **20**, 082514 (2013).
- ²¹ F. W. Perkins, *Nucl. Fusion* **29**, 583 (1989)
- ²² J. R. Myra, D. A. D'Ippolito, and M. J. Gerver, *Nucl. Fusion* **30**, 845 (1990).
- ²³ M. Brambilla, R. Chodura , J. Hoffmann and J. Neuhauser, *Proc. 13th Int. Conf. on Plasma Physics and Controlled Nuclear Fusion Research* (Washington DC, USA, 1990) vol 1 (Vienna, IAEA, 1991) p 723.
- ²⁴ D. A. D'Ippolito, J. R. Myra, M. Bures and J. Jacquinot, *Plasma Phys. and Controlled Fusion* **33**, 607 (1991).
- ²⁵ J. R. Myra, D. A. D'Ippolito and M. Bures, *Phys. Plasmas* **1**, 2890 (1994).
- ²⁶ D. A. D'Ippolito, J. R. Myra, E. F. Jaeger, and L. A. Berry, *Phys. Plasmas* **15**, 102501 (2008).
- ²⁷ D. A. D'Ippolito and J. R. Myra, *Phys. Plasmas* **13**, 102508 (2006).
- ²⁸ E. F. Jaeger, L. A. Berry, J. S. Tolliver, and D. B. Batchelor, *Phys. Plasmas* **2**, 2597 (1995).
- ²⁹ G. Bekefi, *Radiation Processes in Plasmas*, Wiley (1966).
- ³⁰ K. Takayama, H. Ikegami, and S. Miyazaki, *Phys. Rev. Lett.* **5**, 238 (1960).
- ³¹ R. L. Stenzel, *Phys. Rev. Lett.* **60**, 704 (1988).
- ³² R. Chodura, *Phys. Fluids* **25**, 1628 (1982).
- ³³ R. H. Cohen and D. D. Ryutov, *Phys. Plasmas* **5**, 808 (1998).
- ³⁴ K.-U. Riemann, *Phys. Plasmas* **1**, 552 (1994).
- ³⁵ R. Chalise and R. Khanal, *Plasma Phys. Control. Fusion* **54**, 095006 (2012).
- ³⁶ M. M. Hatami, *Phys. Plasmas* **20**, 083501 (2013).
- ³⁷ J. Ou and J. Yang, *Phys. Plasmas* **19**, 113504 (2012).
- ³⁸ P.C. Stangeby, *Nucl. Fusion* **52**, 083012 (2012).
- ³⁹ D. D. Tskhakaya Sr. and L. Kos, *Phys. Plasmas* **21**, 102115 (2014).
- ⁴⁰ M. A. Lieberman, *IEEE Trans. Plasma Sci.* **16**, 638 (1988).
- ⁴¹ V. A. Godyak and N. Sternberg, *Phys. Rev. A* **42**, 2299 (1990).
- ⁴² W. Gekelman, M. Barnes, S. Vincena, and P. Pribyl, *Phys. Rev. Lett.* **103**, 045003 (2009).
- ⁴³ T. G. Jenkins and D. N. Smithe, *Plasma Sources Science and Technology*, (in press).
- ⁴⁴ M. M. Turner and P. Chabert, *Appl. Phys. Lett.* **104**, 164102 (2014).
- ⁴⁵ D. A. D'Ippolito and J. R. Myra, *Phys. Plasmas* **3**, 420 (1996).